Journal of Manufacturing Processes 62 (2021) 275–282

Contents lists available at ScienceDirect

Journal of Manufacturing Processes

journal homepage: www.elsevier.com/locate/manpro

# An optical tomographic method to characterize the mist distribution in MQL Tools

Jay K. Raval, Bruce L. Tai *

*Department of Mechanical Engineering, Texas A&M University, College Station, TX, 77840, USA*

ARTICLE INFO

*Keywords:*
MQL
Optical Tomography
Drilling
Multiphase flow visualization
Filtered Back Projection

ABSTRACT

Proper mist flow is important to Minimum Quantity Lubrication (MQL) machining as only a small amount of lubricant-air mixture is applied to the cutting zone. This paper presents an optical-tomography-based method to visualize the lubricant distribution of MQL mist flow in through-tool channels, particularly for drilling. High-speed images of the flow are acquired from multiple view angles to capture the 2D projections of 3D flow. The Filter Back Projection (FBP) algorithm is used to perform tomography and produce tomographic reconstruction image of the lubricant distribution in the through-tool channels. The method is validated with a known annular flow created using a vertical pipe flow. The method is also applied to two 3D printed drill bits, one with two straight channels and another with two helical channels to emulate actual through-tool channel geometries of drills. The tomographic reconstructions obtained using FBP match with the literature and show a clear influence of the channel geometry on the lubricant distribution. Physical, imaging, and lighting requirements to achieve proper results using this technique are also detailed in the paper.

## 1. Introduction

Minimum Quantity Lubrication (MQL) is a sustainable manufacturing process which helps in reducing the adverse environmental effects [1,2]. An aerosol/mist of air and lubricant is formed using pressurized air and delivered to the cutting zone. The lubricant flow rate ranges from 10 to 500 ml/hr for most practical applications, and the average droplet size depending on the type of system varies from 3 to 50 μm [3–5]. MQL reduces the heat generated due to friction and improves tool life by providing thin film lubrication. Also, small droplets increase the surface area to volume ratio and improve cooling efficiency. However, the cooling capacity is limited by the low quantity of lubricant used and thus the cooling effect is lower compared to water-based coolants. Studies have been performed to evaluate MQL and concluded that MQL can potentially reduce the machining cost by up to 20 % with better surface finish with a similar tool life [5,6]. Therefore, most of the high volume automobile parts are produced using MQL [6].

The efficiency of MQL process is dependent on the quality of the mist. Unlike flood cooling where the cutting interface is always flooded with coolantbecause of small amount of lubricant used in MQL, it is important to deliver it precisely over the cutting edges. In operations like turning and face milling where the cutting zone is easily accessible, external MQL systems employing nozzles are used. Multiple studies have been conducted to analyze the effect of nozzle orientation and location on the cutting performance for turning [7–14]. They have concluded that the nozzle orientation and location are critical parameters for the effectiveness of MQL, as they directly control the mist distribution on the cutting zone. The optimal location for the nozzle is as close to the cutting zone as possible and the orientation should be such that the nozzle is directed towards the rake face of the tool. While in end milling and especially drilling, the cutting zone is inaccessible and through-tool channels are needed to efficiently deliver the mist [15]. Studies have shown changes in the cutting performance with changes in through-tool channel geometry [16–19]. Proper through-tool channel design is an important factor in cutting performance [20]. However, a complete understanding of the lubricating effectiveness with changes in channel geometry is not yet available.

Currently the quality of the mist is determined by measuring droplet

*Abbreviations:* MQL, Minimum Quantity Lubrication; PIV, Particle Image Velocimetry; PDA, Phase Doppler Anemometry; MRI, Magnetic Resonance Imaging; SPECT, Single Photon Emission Computed Tomography; PET, Positron Emission Tomography; PLC, Programmable Logic Controller; BOM, Bill of Materials; SLA, Stereolithography; CCD, Charged Couple Device; BP, Back Projection; FBP, Filtered Back Projection.

* Corresponding author.
*E-mail address:* btai@tamu.edu (B.L. Tai).

https://doi.org/10.1016/j.jmapro.2020.12.025
Received 10 June 2020; Received in revised form 23 October 2020; Accepted 9 December 2020
Available online 29 December 2020

size and droplet velocity [4,21–26]. Contact-based methods are simple but inapplicable to small channel sizes (1− to 2 mm). The flow would be disrupted due to the equipment, leading to inaccurate results. Therefore, non-contact measurement techniques are preferred. Particle Image Velocimetry (PIV), Phase Doppler Anemometry (PDA), and jet impingement are the most common methods used to measure velocity. PIV and PDA are planar measurements, which illuminate a plane of the flow using laser sheet optics to capture the tracer particles. PIV compares multiple consecutive images to track the motion of droplets and thereby calculate the velocity. PDA uses the change in frequency of radiant and reflected laser (Doppler Effect) to estimate the velocity. However, these methods are incapable of handling highly turbulent flow like MQL where out of plane motion can lead to data loss. The jet impingement technique uses a force sensor to measure the average force and uses the measured force and flow rate to estimate the flow velocity. The measurement of droplet sizes is performed using image processing and wavelet transform. The mist impinges for a very short period on a glass plate and the droplets are allowed to deposit on the plate. An image of the droplets is used to estimate the droplet size and volume [25]. However, droplet velocity and size alone do not provide any information about the lubricant distribution in the flow. A previous study by the authors has shown heterogeneous mist distribution in the channel, which can potentially affect lubricant coverage [27]. Before studying the lubricant distribution on the cutting edge, it is necessary to determine the lubricant distribution in the through-tool channels, which is the focus of this study.

Since the channel is long, the flow should be fully developed near the exit of the channel, meaning that the lubricant distribution is not a function of the channel length. Therefore, the lubricant distribution at the exit of the channel should accurately represent the lubricant distribution inside the channel. In this study, a tomography technique is used to measure the lubricant distribution at the exit of through-tool channels. There are multiple tomographic techniques available with each having its pros and cons [28,29]. If the whole 3D control volume is being reconstructed, it is called 3D imaging and if only a cross-section is being reconstructed then it is called 2D imaging. Tomography techniques analyze the composition of phases inside the control volume and provide the local phase distribution. These techniques are categorized based on the type of source and the signal used to respectively excite and capture information about the control volume. A tomographic system consists of a source and a receiver. The source emits irradiance (excitation) and the receiver captures the signal (response). The emitted signal can be either of electromagnetic waves, acoustic waves, or photonic waves. The characterization of the control volume is based on the signal used to capture the flow. It can be either local emissivity, transmissivity and/or reflectivity [29]. All materials behave differently under different excitations. For example, metals, which are opaque to optical light, are translucent to X-ray excitation. Therefore, the selection of an excitation source depends on the type of body to be studied, type of radiation, physical constraints, and the required level of accuracy. Table 1 summarizes and compares the most common tomography techniques [30]. The machining environment consists of metal tools and structures and is performed in open air environment. These conditions impose constrains on the tomographic method. Therefore, based on these constraints and the required quality of results, optical tomography was selected to capture the flow distribution. Detailed discussion for this selection is explained in Sec. 2.1.

**Table 1**
Comparison of different tomography techniques.

| Name | Contrast | Spatial Resolution | Temporal Resolution |
|---|---|---|---|
| Computed Tomography | Attenuation coefficient, Density | 0.4−0.6 mm | 1−2s |
| MRI | Amplitude of magnetization | 0.5 mm | 0.1−10 s |
| SPECT/PET | Tracer particle concentration | 3−20 mm | 5−10 min |
| Optical Tomography | Reflection/ Attenuation co eff. | 0.01−10 mm | 0.1−10 s |
| Microwave Tomography | Refractive index | 1/10 of wavelength | 0.01−10 s |
| Impedance Tomography | Impedance/ Resistance | 3−10 % of diameter | 0.001−0.01s |

In this paper a new optical tomography based method for visualizing the lubricant distribution in the through-tool channels is presented. To structure the paper, section 2 contains information about the tomographic method selection, physical experimental setup, image acquisition and imaging settings. Section 3 briefs about the algorithm used for tomographic reconstruction and the validation study for the proposed method. Section 4 includes case studies using the proposed method. Section 5 includes discussion about the proposed method and lastly, section 6 concludes the paper.

## 2. Experimental setup and measurement method

### 2.1. Selection of the tomographic technique

As mentioned earlier, the physical and technical constraints play an important role in the selection of proper tomographic technique. Fluid velocity ranging up to 300 m/s require a technique with high temporal resolution. And droplet sizes as small as 1 μm require high spatial resolution. Among all the tomographic techniques mentioned in Table 1, Magnetic Resonance Imaging (MRI), Impedance Tomography, and Optical Tomography are the most viable techniques given their spatial and temporal resolutions. However, since MRI uses high powered electromagnets for generating excitation, it is not a feasible option around metal machines. Impedance Tomography is also not a feasible option because of the noise generated in an air environment. In comparison, Optical Tomography, which uses light as excitation, is safer and the most applicable option. It requires a translucent medium, and thus can only be applied when the drill bit is not inside the hole. For the above reasons, optical tomography was selected for studying the lubricant distribution. The excitation waves used for optical tomography can be divided into two categories: coherent light and incoherent light. The use of coherent light (i.e., laser) can have an extremely high spatial and temporal resolution by pulsed excitation and the time encoding technique. However, such a complex and high-cost setup is unnecessary for this current work since the objective is not to capture individual droplets. Therefore, a non-coherent white light tomography is used in the paper. Since the reflective intensity of the lubricant and air differ by order of magnitudes, the difference between these phases is clear. By assuming that the reflective intensity is directly proportional to the local density, the reconstructed image shows the distribution of the lubricant in the flow, termed as flow distribution. The next section shows the physical setup and arrangement of equipment used for this study.

### 2.2. MQL system setup

The experimental setup aiming to simulate a realistic MQL mist flow is shown in Fig. 1(a). The setup consists of a production level dual-channel MQL system (Model: Infinity, Unist Inc., MI), servo motors, rotary union, light source, and a high-speed camera (Model: Phantom MiroLab 310, Vision Research, NJ). The MQL system is equipped with a close loop servo controlled positive displacement pump, providing consistent steady state lubricant flow along with accurate control over the lubricant flow rate. This feature is important not only for its practicality in production but also for offering a nearly steady-state flow during the course of measurement. In this system, a solenoid valve is placed near the spindle for the lubricant tube as well as the air channel, providing individual control over both the flows. The valve remains shut while the system is off to keep the tubes pressurized and opens as soon as the system is turned on. This improves the response time of the MQL

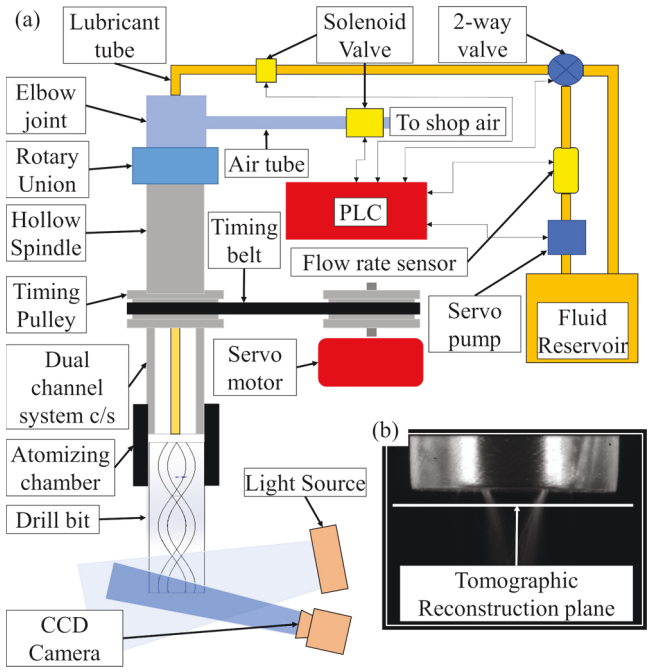


**Fig. 1.** (a) Schematic of the experimental setup (b) Sample image acquired using the high-speed CCD camera.

system and provides instantaneous flow. Castrol Hyspray A1536, a fatty-alcohol based oil is used as the lubricant. The properties of the lubricant are summarized in Table 2. It is the standard Bill of Materials (BOM) oil for high volume automobile parts MQL machining. A servo motor is used to control the spindle speed as well as the angular position of the drill (for imaging). The rotary union allows the shaft to rotate without rotating the tubing for MQL. Two 100 W white LED light arrays are used to provide irradiance. The high-speed camera is capable of capturing 1080p 8-bit gray scale images at 3200 fps and is used for image acquisition. Fig. 1(b) shows a sample image of the flow captured using it. A black background is set up around the drill to avoid any reflection from the surrounding objects in addition to the use of a dark room. This reduces the noise in the image and ensures that only the light reflected from the flow is captured by the camera. The intensity of the reflected light determines the intensity of the pixel and is used as the signal for determining the local lubricant distribution. The drills are additively manufactured using Form 2 (Formlabs, Boston, MA) Stereolithography (SLA) machine. Additive manufacturing is chosen for the flexibility in channel design obtained. This allowed the use of non-standard channel shapes and locations for testing and verification purposes. The SLA process is chosen because of its capability to provide high resolution (about 100 μm in x and y and 25 μm in z-direction) and finish (Ra < 1 μm) compared to other additive manufacturing processes. Formlabs' proprietary clear resin used for the printing the drills had a similar surface energy to that of carbide drills. The contact angles for lubricant and clear resin are 15°-18° which is similar to that between the lubricant and carbide tool i.e. 10° - 20° [5,23]. Both the measurements were performed using the sessile drop method.

MQL is a multiphase flow containing air and lubricant. Air is optically clear and does not reflect optical light, while the lubricant is translucent and reflects light. Therefore, using optical light as irradiance and a CCD camera for capturing the reflected light, the distribution of the lubricant can be isolated from the total flow. MQL droplets reflects some of the light and scatter a small portion of it, while the rest is transmitted through, as illustrated by the top view in Fig. 2. This effect is cumulated for multiple droplets and then the total reflected and scattered light is captured by the array of sensors on the CCD camera. Each image captured by the camera is a 2D projection of a 3D domain. The higher intensity means a higher density of lubricant in the flow, as illustrated by the front view in Fig. 2. Multiple 2D projected images can be used to reconstruct the 3D lubricant distribution. In this study, the reconstruction is only needed on a plane (namely reconstruction plane), which is a line in 2D view. The flow distribution on the reconstruction plane provides the flow distribution inside the through-tool channels. Note the reconstruction of 3D flow is possible but not necessary for this work.

**Table 2**
Material properties for Castrol Hyspray A1536.

| Property | Measurement Standard | Unit | Value |
|---|---|---|---|
| Viscosity @40°C | DIN 51562 | $mm^2/s$ | 28 |
| Viscosity @100°F | ASTM D446 | SUS | 148 |
| Flash Point | ISO 2592 | °C | 194 |
| Density @20°C | – | $kg/m^3$ | 838 |

### 2.3. Image acquisition and pre-processing

The intensity of each pixel on the captured 2D image is proportional to the cumulative flow density in the direction normal to the pixel. The information can be described by the Radon transform function, which describes the 2D projection of 3D objects for waves travelling through the object. Radon transform is essentially the integral summation of all the function values along a line. Fig. 3 shows the schematic for the Radon transform. For example, Fig. 3(a) is a body where the density is homogeneously distributed on a plane and is mathematically represented as $f(x, y)$. To find the projection at a known angle $\theta$, the local density is integrated along the direction of projection (i.e., the normal direction to a pixel). Since projections at multiple angles are needed, it is easier to work with a coordinate system that is aligned with the camera sensor. Therefore, the part coordinate system (x, y) is converted to the sensor coordinate (p, q) using the rotation of frames. The relation between these frames is shown in Eq. 1. For a fixed projection angle ($\theta$) and fixed sensor position ($p$), the total signal intensity is the integration of densities along the projection direction with $q$ ranging from -∞ (source) to 0 (sensor). The function that describes the total intensity at given sensor location ($p$) and projection angle ($\theta$) is known as the Radon transform function ($Rf(p, \theta)$), which is given in Eq. 2. The projection of a homogenous circular body is illustrated in Fig. 3(a), which has higher signal intensity at the location through the diameter and lower signal intensity near the extreme points. Fig. 3(b) shows a body with two inhomogeneity patches, one with a higher density and other with lower density. The high-density patch produces a stronger signal projected to the sensor array while the low-density region produces a weaker signal. Therefore, a difference in the Radon transform function of both bodies can be easily observed. With the same concept, wherever more lubricant

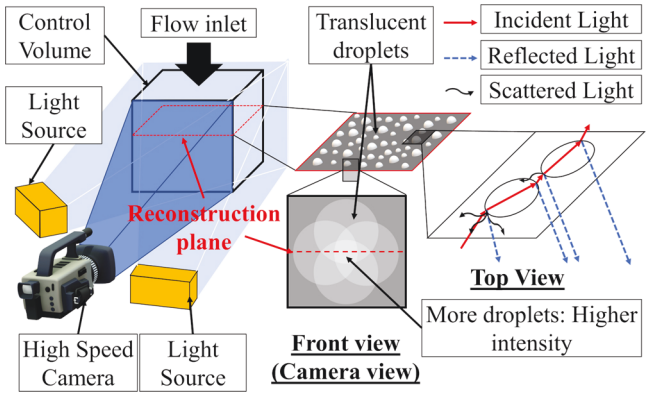


**Fig. 2.** Orientation of lights and camera, interaction of light with the droplets and integration of reflected light intensity due to 2D projection of 3D flow.

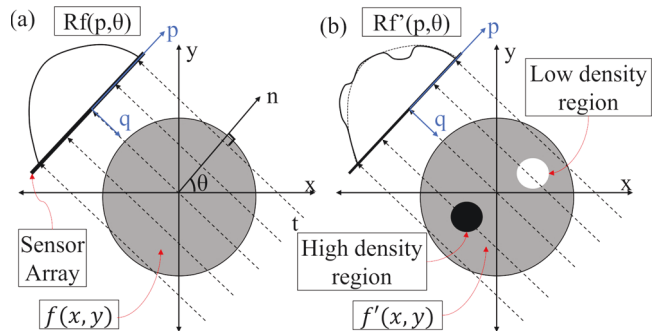


**Fig. 3.** (a) Radon transform of a body with homogeneous density distribution (b) Radon transform of a body with presence of inhomogeneity in the density distribution.

droplets are present in the mist flow, the signal intensity is higher and vice versa. A complete Radon transform function would contain information from multiple view angles and can be post-processed by a tomographic reconstruction algorithm to find the local density distribution (explained in Sec 3: Algorithm).

$$(x(q), y(q)) = (qsin\theta + p\,cos\theta, \quad -qcos\theta + psin\theta) \tag{1}$$

$$Rf(p,\theta) = \int_{-\infty}^{0} f(x(q), y(q))dq \tag{2}$$

### 2.4. Light and camera settings

A single Phantom MiroLab 310 camera along with two 100 W LED light sources, was used for image acquisition. The camera is positioned to capture a control volume of size 10 mm × 10 mm × 10 mm and the lights are on either side of the camera pointing towards the control volume. Projections of the lubricant distribution at multiple angles are obtained by synchronizing the spindle speed of the drill and the frame rate of the camera. This method of image acquisition is called sequential imaging. For example, the drill is rotating at 360 RPM, i.e. 6 RPS. If the camera frame rate is kept at 1080 fps, between each consecutive frame the drill will rotate by 2 degrees. The angular difference between each consecutive frame determines the difference between the projections and is defined as discreteness. If the angle is too small the consecutive projections will be very similar and become redundant. With the frame rate and drill speed fixed, the aperture, irradiance, and the exposure of the camera must be fixed and carefully set up. The irradiance intensity should be high to have enough intensity of the reflected light and avoid any attenuation through the control volume. The best results for irradiance are obtained when there are multiple light sources all around the control volume. If only a limited number of light sources available, the best location for the light source is right beside the camera. The aperture should be kept as large as possible. A larger aperture allows more light to enter into the camera and therefore improves the signal-to-noise ratio. However, increasing the aperture reduces the depth of field. The selection of aperture should be a trade-off between getting sufficient light into the camera and keeping the whole control volume in focus. The exposure time of each frame should be as long as possible to allow more light into the camera and improve the signal to noise ratio. A long exposure time captures the pathlines of the droplets instead of the individual droplets. This is beneficial to this sequential imaging method because the instantaneous droplet distribution differs from angle to angle. Unless all the projection images are acquired simultaneously, the droplet distribution captured in each projection will be different, and tomographic reconstruction won't be possible. The use of long exposure time facilitates with flow averaging and mitigates the effect of instantaneous change in droplet locations generated because of sequential imaging. The comparison between long and short exposures is shown in

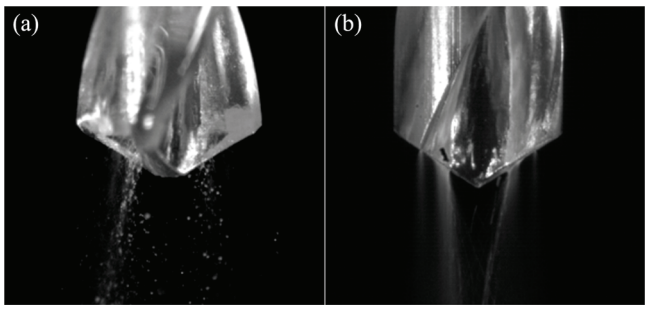


**Fig. 4.** (a) Image captured using short exposure time (4 μs) (b) Image captured using long exposure time (900 μs).

Fig. 4. Fig. 4(a) shows an image captured with 4 μs exposure time while Fig. 4(b) shows an image captured with 900 μs exposure time. The use of short exposure time captures individual droplets while the use of long exposure time captures the pathlines of the droplets. When individual droplets are captured in the images, no solution can be obtained when tomography techniques are used. The use of long exposure times facilitates averaging and helps generating a stable tomographic solution.

However, it should be noted that the frame rate limits the maximum exposure time that can be used. Exposure time should be long enough to see the flow pathlines but should be lower than the frame rate to maintain discreteness in the image acquired at multiple consecutive angles. Lastly, the control volume should be isolated from reflection signals of surrounding objects. A black background and/or a dark room should be used to reduce the noise level. In this study, both the precautions were taken. The black images (locations where the pixel intensity should be theoretically '0' because of no flow) have an average intensity of 4 units on an 8-bit (0–255 units) scale. This determines the uncertainty in the measurement of the flow because of false signal captured by the camera. The maximum experimental uncertainty can be estimated by taking the ratio of noise and the least value of signal. The pixel intensity (of the flow) in the captured images ranges from 50 to 250 units; therefore, the maximum uncertainty in the measurement of lubricant density is about ± 8 % (i.e., 4/50).

## 3. Flow reconstruction method and validation

### 3.1. Algorithm

Image acquisition of the flow defined using Radon transform function is known as the forward problem. While, the process of using the information from 2D projections to generate tomographic reconstruction is known as inverse problem. With an appropriate quantity and quality of images, the lubricant density on the reconstruction plane can be extracted through a system of equations. The tomographic reconstruction is an image where each pixel has a certain coefficient of reflectivity. Since the reflectivity of a pixel is proportional to the number of droplets passing through, the distribution of the reflection coefficient represents the lubricant distribution. The intensities of pixels along the reconstruction plane, which is a line in captured images as highlighted in Fig. 1(b), are extracted for all the viewing angles. Using the data of pixel intensities and the angular location, a sinogram (i.e., the plot of Radon transform function) for the projections can be generated. An example is shown in Fig. 5, where Fig. 5(a) shows a Shepp-Logan phantom (a standard image for testing purposes) is converted to a sinogram (Fig. 5(b)). On the sinogram, y-axis shows the projection angle ($\theta$, 0° to 360°) and x-axis shows the location of the pixels ($p$) along the reconstruction line of each captured image. This sinogram is used to generate the system of equations (Eq. (3)); solving for $\mathbf{x}$ will yield a 2D cross-sectional lubricant distribution.

$$\mathbf{W}_{m\times n^2}.\mathbf{x}_{n^2\times 1} = \mathbf{P}_{m\times 1} \tag{3}$$

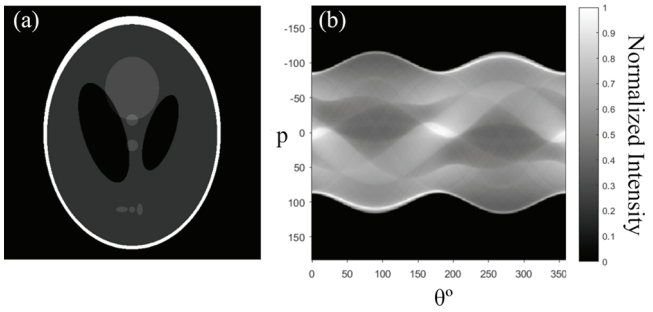


**Fig. 5.** (a) Shepp-Logan phantom image (b) Sinogram obtained using Radon transform.

In Eq. (3), **P** is the projection vector, where each element is the projection intensity experimentally captured (i.e., the data in the sinogram). The size of the projection vector is $m$, which is equal to $i \times j$ where $i$ is the number of projection angles and $j$ is the number of pixels on the projection of reconstruction plane. Vector **x**, which includes the reflection coefficient of each pixel; therefore, for an $n \times n$ size reconstructed image, the size of **x** is $n^2 \times 1$. The weight matrix **W**, is used to identify the pixels contributing to a particular projection. Its size depends on the number of projection angles and the number of sensors (pixels) on the camera. **W** is usually a non-square matrix and therefore direct inversion for obtaining the solution is not possible. The elements of **W** give the particular pixel's contribution to the projection. The coefficients of **W** are calculated automatically by the reconstruction algorithm explained later in this section. Fig. 6 shows a schematic explaining the calculation of coefficients for the elements of **W**. The reconstruction image is of size $3 \times 3$. Only the pixels along the highlighted ray (pixel no. 2, 3 and 6) will have non-zero coefficient values, while others will have a zero coefficient value for the particular sensor (i.e. fixed $\theta$ and $p$ values). The proportion of the area of the pixel contributing to the projection is used as the coefficient value.

Since $m < n^2$ is always true for practical applications, the system of equations is always under-constrained, and thus there exists multiple solutions for the system of equations. Therefore, a proper algorithm called tomographic method is required to generate the most feasible solution [28,29]. They require the axis of rotation to be aligned with the center of the image. Since direct proportionality is assumed between the intensity of each pixel and the lubricant density in the direction normal to the pixel, Back Projection (BP), an analytical method based on the inversion of Radon transform, can be used here. BP assumes that the beam of light travels in a straight line, each line is parallel to each other, and the center of the image is aligned with the axis of rotation. However, BP can lead to a faded image with no clear boundaries, Filtered Back Projection (FBP), a modified BP technique, is adopted which uses a ramp filter to regain the sharpness of the image and can generate sharper tomographic reconstructions [31]. MATLAB's image processing toolbox's inbuilt function, 'iradon' (Inverse Radon) is a FBP based method

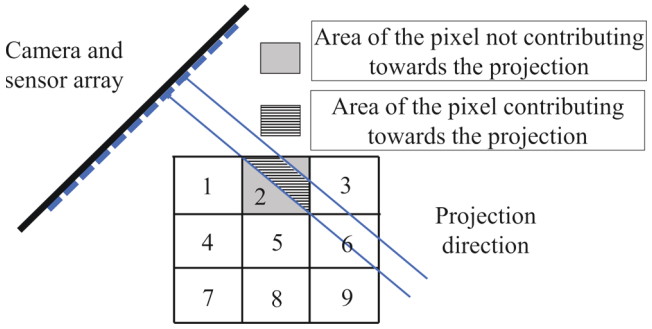


**Fig. 6.** Calculation of coefficients for the weight matrix W.

which uses the sinogram as an input and generates tomographic reconstruction image. For the example of Shepp-Logan phantom image in Fig. 5(a), data in the sinogram (Fig. 5(b)) is used to generate tomographic reconstructions using FBP with different number of projections shown in Fig. 7. These results were used to verify and troubleshoot the reconstruction code and test for the effect of number of projection angles on the reconstruction quality. As the results show in Fig. 7(a–f), increasing the number of projection angles improves the details in the reconstructed image. The best image is obtained for 360 projections.

### 3.2. Validation

The proposed method was validated against a known result of a two-phase flow. A cylinder of 9.525 mm (3/8″) diameter with a circular channel in the center was designed and 3D printed (Fig. 8(a)). The channel size was 3 mm in diameter and the channel length is 70 mm. The flow rate was kept as 200 mL/hr. The drill was rotating at 360 RPM and image acquisition was carried out 1080 fps with 900 μs exposure time. This produced 180 projections around the drill, each 2° apart. These 180 projections were used to generate the tomographic reconstruction using the FBP method as mentioned in Section 3.1. Fig. 8(b) shows sample images captured at different angles for the given case and Fig. 8(c) shows the tomographic reconstructed image. The reconstruction was carried out at the reconstruction plane highlighted in Fig. 2 as well as in the sample images in Fig. 8(b). As seen in Fig. 8(c) the high lubricant density regions are clearly near the periphery of the channel which is an annular type of flow. The red circle shows the channel boundary and was added for visualization purposes. From published data, the air speed in the through-tool channels can reach up to 300 m/s for a 2 mm channel diameter and a further increase in the channel diameter produces only marginal change in the flow velocity [32]. Therefore, it is safe to assume that the flow speed in the validation design channel is also in the same range. The Reynolds number for the channel is of the order of 30,000. Based upon the flow velocity and the constituent phase proportion ratio (the lubricant to air ratio was found less than 0.01 %), highly turbulent flow with annular flow distribution is expected in such a vertical pipe, and thus the majority of the lubricant is flowing at the periphery of the channel [33,34]. This type of flow is observed because of the high adhesion forces between the lubricant and the channel (high surface energy) and trapping of the denser lubricant particles in the boundary layer. Therefore, the results obtained by the method closely match with the expected results for the type of flow.

## 4. Case studies

### 4.1. Effect of channel geometries

The proposed method was applied to two other cases to represent

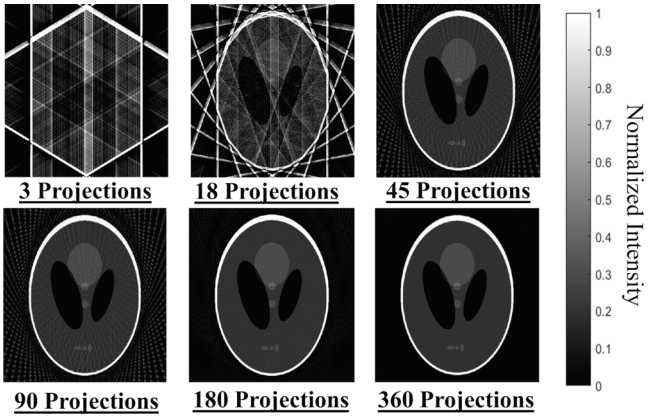


**Fig. 7.** Tomographic reconstructions using FBP at different no of projections.

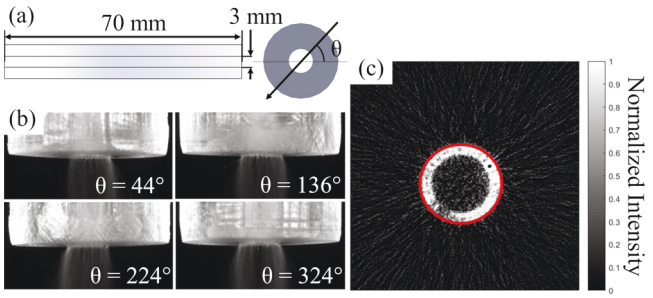


**Fig. 8.** Flow through a vertical pipe (a) Geometry of the channel (b) Sample images captured using image acquisition technique at different projection angles (c) Tomographic reconstruction using FBP technique.

actual drill bit designs. The drill geometry shown in Fig. 9(a) has two straight circular channels at a fixed radius from the axis of rotation. This type of channel geometry is observed in straight flute drills. Unlike the design used for validation purposes, the two circular channels placed are at a fixed radius of 2.5 mm from the axis. A mixing region is added to the entry of the channels to ensure that both channels have the same flow rate. The channel diameter is changed to 2 mm while the channel length is still 70 mm. The flow and imaging conditions were kept the same as the validation experiment. Fig. 9(b) shows the sample images captured at different projection angles. As seen in tomographic reconstruction (Fig. 9(c)), when the channels are moved away from the axis of rotation, the lubricant distribution still somewhat remains annular. However, the reconstruction is not as well defined as that of the single-channel drill. Since the lubricant distribution still remains annular, it means that the centrifugal forces generated because of the rotation of the drill are not high enough to change the lubricant distribution pattern.

The second case represents a drill with helical channels. The geometry of the drill is shown in Fig. 10(a). The radial location and channel size were kept the same as the previous case, but the channels followed a helical path. The helix angle was kept as 30° based upon the common value used for commercial drills. Fig. 10(b) shows sample images captured at different angles and a clear change in the projected distribution can be seen with the change in projection angle. As seen in the tomographic reconstruction in Fig. 10(c), with the inclusion of the helix angle, the high flow concentration region shifts towards the axis of rotation of the drill, and the flow distribution does not remain annular anymore. Unlike Fig. 9(c) where high flow concentrations were observed all around the periphery of the channel, Fig. 10(c) shows only a few spots where high concentration regions are observed albeit still at the periphery of the channel. This change in the flow distribution changes the flow regime and thus the flow distribution does not remain annular anymore. This means that the helix angle does have a significant effect on the flow distribution. The flow is forced to swirl around the axis of rotation and thus the flow pattern changes. The results obtained match with the result predicted by the authors in their previous study

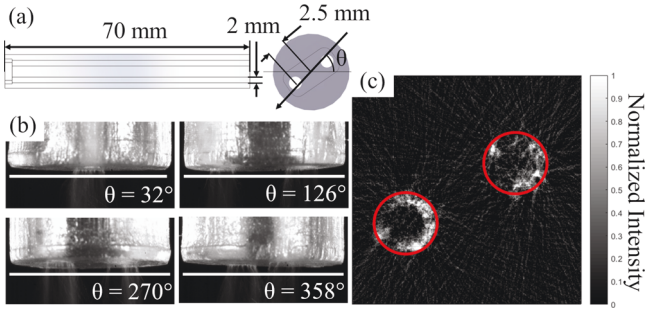


**Fig. 9.** Dual straight channel drill design (a) Geometry of the channel (b) Sample images captured using image acquisition technique at different projection angles (c) Tomographic reconstruction using FBP technique.

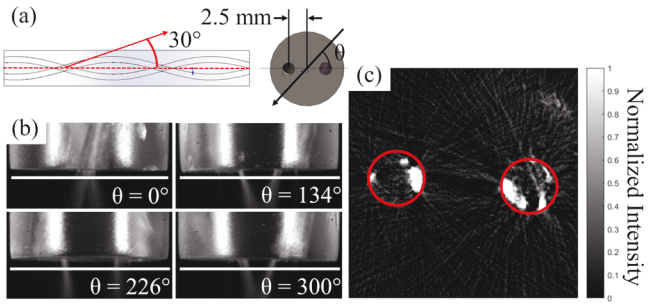


**Fig. 10.** Dual helical channel drill design (a) Geometry of the channel (b) Sample images captured using image acquisition technique at different projection angles (c) Tomographic reconstruction using FBP technique.

[27].

### 4.2. Increasing the number of projections

Theoretically, higher the number of projections better the quality of the reconstruction image. However, this is only the case if the object under study is stationary during the image acquisition. For our case, sequential imaging is used. The drill is rotating at a constant velocity and a long exposure time (900 μs) is used for image acquisition; therefore, the drill moves by a small angle during image acquisition. This leads to non-discreteness in image acquisition. Therefore, it is necessary to evaluate the effect of this physical constraint on the reconstructed image. Using the same oil flow rate (200 mL/hr.) and helical channel geometry shown in Fig. 10(a), tomographic reconstruction was performed with 180 projections and 360 projections. These correspond to the frame rates of 1080 fps and 2160 fps, respectively, at a constant spindle speed of 360 RPM. The exposure times used were 900 μs and 460 μs, respectively, limited by the frame rate. Each projection was 1° apart for 2160 fps, while it was 2° apart for 1080 fps. Fig. 11(a) shows the tomographic reconstruction results using 180 projections and Fig. 11(b) shows the tomographic reconstruction using 360 projections.

As seen, the quality of details in tomographic lubricant distribution in both the images varies. The channel location on both the reconstruction images is different because the reference angle used was different but that does not affect the result. For the case of 360 projections, circular artefacts (arcs) appear in the reconstruction which is not seen for the 180 projections case. Furthermore, 180 projections shows more lubricant concentration zones then 360 projections because, the longer exposure time used improved the signal to noise ratio. Therefore, 180 projections provide clearer results as compared to 360 projections for this method because of the sequential image acquisition approach used.

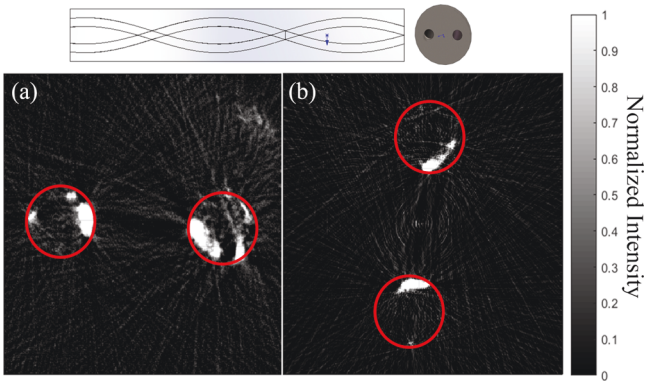


**Fig. 11.** Dual helical channel drill design (a) Tomographic reconstruction using 180 projections (b) Tomographic reconstruction using 360 projections.

## 5. Discussion

The tomographic reconstruction for the verification design shows very well defined annular flow. High lubricant concentration regions are close to channel periphery. However, the reconstruction for the two-channel straight design is not as well defined. This is because, for the later the total flow rate was divided into two channels and thus fewer droplets were in each channel to reflect light. If the flow rate increases, proper lubricant reconstruction is expected; however, the excessive flow rate may also change the flow regime and results obtained will be of no practical importance. Nevertheless, when the channel are shifted from the axis of rotation, the lubricant distribution remains annular because, the velocity in the axial direction is high, providing higher momentum along the axial direction as compared to the momentum imparted by the centrifugal forces in the radial direction due to drill rotation. If the rotational speed of the drill is increased or if the channels are moved away from the axis of rotation, the centrifugal force effect may become noticeable on lubricant distribution. For the case of the helical channel, the lubricant distribution does not remain annular anymore, though the radial distance of the channels and the drill rotational speed are identical to those of the straight channel drill. Therefore, it is evidenced that the helical path does have a significant effect on lubricant distribution. The helical channel generates secondary vortices inside the channel which disrupts the annular lubricant distribution [35].

For the evaluation of the number of projection angles, unlike the simulation result of the Sheep-Logan phantom, 180 projections provided a better reconstructed image than that of the 360 projections. There can be two possible explanations for the issue, (i) the flow not being steady state or (ii) the dynamic motion of the drill while capturing an image. It was verified that the flow was steady state since the flow rate remained constant throughout the experiment. Therefore the dynamic state of the drill has adverse effect on the image quality. Because of the longer exposure time and angularly wide spaced projections (discrete) for 180 projections. During the actual image acquisition, the drill rotates at a constant speed whereas the phantom image is stationary at all time. When 2160 fps is used, each projection is 1° apart while it is 2° apart for 1080 fps. The larger angle between the projections improves the discreteness in the projections. For 360 projections, by the time the image acquisition at angle $x^\circ$ ends the drill is already close to the position for image acquisition at angle $x^\circ+1^\circ$. While, for 180 projections, there is some time between the end of image acquisition for angle $x^\circ$ and start of angle $x^\circ+2^\circ$ Therefore, although more projections are theoretically better, it may have a negative effect if the object is in a dynamic condition when performing sequential imaging.

The proposed methods still has some limitations which need to be dealt to improve the accuracy of the method. Currently, the maximum size of the control volume is limited because, for a larger control volume, the assumption of homogeneous irradiance does not hold. Further calibration and tests are required to consider the attenuation in the irradiance as the size of the control volume increases. Also, the method can only differentiate high droplet concentration regions since the signal from low contrast regions is extremely low. Further, the method utilizes sequential imaging and thus needs to employ long exposure times. This limits the capacity to capture the individual droplets and to reconstruct a detailed droplet distribution. If multiple cameras are used surrounding the control volume, instantaneous imaging can be performed and detailed lubricant distribution containing individual droplets can be obtained.

## 6. Conclusion

The proposed optical tomography technique provides reasonable results to visualize the mist flow distribution. The method is economical and practical as it only requires a non-coherent optical light source, a high-speed camera of 1000–2000 fps, and it uses an open-source algorithm for tomographic image reconstruction. The image acquisition takes about 0.15 s and the solution algorithm takes about 0.1 s to generate the tomographic image. The process provides means to experimentally measure the flow distribution inside the channel, which can be used as the initial flow condition when simulating oil coverage on the cutting edge. Then, the data obtained from the tomographic reconstruction about the flow distribution helps to analyze the effect of different channel shapes, which bridges the gap between the drill performance and channel geometry.

Learning from the experimental work, several restrictions must be considered while setting up the measurement. First, since no attenuation in the irradiant light is assumed, the size of the control volume should be as small as possible. Second, the lighting condition should be as homogenous as possible. Third, the axis of rotation needs to be aligned with the center of the image for the reconstruction algorithm to work. Lastly, the exposure time should be long enough to see a nearly steady flow instead of individual droplets. Good quality of captured images is the key to a successful reconstruction result.

## Declaration of Competing Interest

The authors declare that they have no known competing financial interests or personal relationships that could have appeared to influence the work reported in this paper.

## Acknowledgements

The authors would like to thank Unist Inc. (Grand Rapids, MI), for providing the industrial scale Infinity system at discount and NSF for funding the project through grant #1760985. We would also like to thank Mr. Tim Bangma (Unist Inc.) for providing technical support with the Infinity system, Dr. Dave Stephenson (Ford Motor Company) and Dr. Yi-Tang Kao (Saint Gobain) for their technical assistance, and Mr. Aamer Kazi (Texas A&M University) for his help with proof reading of the document.

## References

[1] Chen Z, et al. Analysis of cutting fluid aerosol generation for environmentally responsible machining. CIRP Annals 2000;49(1):53–6.
[2] Tai B, et al. Minimum quantity lubrication for sustainable machining. 2017.
[3] Li Q, et al. Characterization of micromist for effective machining. 2015 (57359): p. V02AT02A058.
[4] Dasch J, Kurgin S. A characterisation of mist generated from minimum quantity lubrication (MQL) compared to wet machining. Int J Mach Mach Mater 2010;7.
[5] Tai BL, Dasch JM, Shih AJ. Evaluation and comparison of lubricant properties in Minimum Quantity Lubrication machining. Mach Sci Technol 2011;15(4):376–91.
[6] Tai BL, et al. Minimum quantity lubrication (MQL) in automotive powertrain machining. Procedia CIRP 2014;14:523–8.
[7] Jang D-y, Jung J, Seok J. Modeling and parameter optimization for cutting energy reduction in MQL milling process. Int J Precis Eng Manuf Technol 2016;3(1):5–12.
[8] Hsu Q-C. Optimization of minimum quantity lubricant conditions and cutting parameters in hard milling of AISI H13 steel. Appl Sci 2016;6(3):83.
[9] Gupta MK, et al. Experimental investigation and optimization on MQL-assisted turning of inconel-718 super alloy. Advanced Manufacturing Technologies. Springer; 2017. p. 237–48.
[10] Gupta MK, Sood P, Sharma VS. Machining parameters optimization of titanium alloy using response surface methodology and particle swarm optimization under minimum-quantity lubrication environment. Mater Manuf Process 2016;31(13): 1671–82.
[11] Masoudi S, et al. Experimental investigation into the effects of nozzle position, workpiece hardness, and tool type in MQL turning of AISI 1045 steel. Mater Manuf Process 2017;33:1011–9.
[12] Zhu G, Yuan S, Chen B. Numerical and experimental optimizations of nozzle distance in minimum quantity lubrication (MQL) milling process. Int J Adv Manuf Technol 2019;101(1):565–78.
[13] Gajrani KK, et al. Hard machining performance of indigenously developed green cutting fluid using flood cooling and minimum quantity cutting fluid. J Clean Prod 2019;206:108–23.
[14] Gajrani KK, Ram D, Sankar MR. Biodegradation and hard machining performance comparison of eco-friendly cutting fluid and mineral oil using flood cooling and minimum quantity cutting fluid techniques. J Clean Prod 2017;165:1420–35.
[15] Khan WA, et al. Through-tool minimum quantity lubrication and effect on machinability. J Manuf Process 2018;34:750–7.
[16] Tai BL, et al. High air pressure in MQL deep Hole drilling workpiece temperature. Advanced materials research. Trans Tech Publ; 2011.

[17] Tai BL, Stephenson DA, Shih AJ. Workpiece temperature during deep-hole drilling of cast Iron Using high air pressure minimum quantity lubrication. J Manuf Sci Eng 2013;135(3).
[18] Tai BL, Stephenson DA, Shih AJ. Thermal modeling of workpiece temperature in MQL deep-Hole drilling. ASME 2010 International Manufacturing Science and Engineering Conference 2010.
[19] Tai BL, Stephenson DA, Shih AJ. An inverse heat transfer method for determining workpiece temperature in minimum quantity lubrication deep hole drilling. J Manuf Sci Eng 2012;134(2):021006–021006-8.
[20] Hughey E, Stephenson DA. Oil delivery balancing and priming for multi-diameter minimum quantity lubrication tooling assemblies. Procedia Manuf 2019;34:343–8.
[21] Stephenson DA, Hughey E, Hasham AA. Air flow and chip removal in minimum quantity lubrication drilling. Procedia Manuf 2019;34:335–42.
[22] López de Lacalle LN, et al. Experimental and numerical investigation of the effect of spray cutting fluids in high speed milling. J Mater Process Technol 2006;172(1):11–5.
[23] Lerma I, et al. Characterization of micromist for effective minimum quantity lubrication. Adv Mat Res 2015;1115:43–6.
[24] Maruda RW, et al. A study on droplets sizes, their distribution and heat exchange for minimum quantity cooling lubrication (MQCL). Int J Mach Tools Manuf 2016;100:81–92.
[25] Park K-H, et al. A study on droplets and their distribution for minimum quantity lubrication (MQL). Int J Mach Tools Manuf 2010;50(9):824–33.
[26] Husted BP, et al. Comparison of PIV and PDA droplet velocity measurement techniques on two high-pressure water mist nozzles. Fire Saf J 2009;44(8):1030–45.
[27] Raval JK, Kao Y-T, Tai BL. Characterizing mist distribution in Through-Tool minimum quantity lubrication drills. J Manuf Sci Eng 2020;142(3).
[28] Gordon R, Bender R, Herman GT. Algebraic Reconstruction Techniques (ART) for three-dimensional electron microscopy and X-ray photography. J Theor Biol 1970;29(3):471–81.
[29] Chaouki J, Larachi F, Duduković MP. Noninvasive tomographic and velocimetric monitoring of multiphase flows. Ind Eng Chem Res 1997;36(11):4476–503.
[30] Grangeat P. Tomography. John Wiley & Sons; 2013.
[31] Gardner RJ. Geometric tomography, Vol. 6. Cambridge: Cambridge University Press; 1995.
[32] Raval JK, Hung WN, Tai BL. Multiphase flow distribution in MQL drilling using optical intensity distribution based approach. In: ASME 2019 14th International Manufacturing Science and Engineering Conference; 2019.
[33] Brennen CE, Brennen CE. Fundamentals of multiphase flow. Cambridge university press; 2005.
[34] Schwarzkopf JD, et al. Multiphase flows with droplets and particles. CRC press; 2011.
[35] Yamamoto K, et al. Flow through a rotating helical pipe with circular cross-section. Int J Heat Fluid Flow 2000;21(2):213–20.